Biosensors and Bioelectronics 220 (2023) 114915

Contents lists available at ScienceDirect

Biosensors and Bioelectronics

journal homepage: www.elsevier.com/locate/bios

Near perfect classification of cardiac biomarker Troponin-I in human serum assisted by SnS_2-CNT composite, explainable ML, and operating-voltage-selection-algorithm

Partha Pratim Goswami, Tushar Deshpande, Dinesh Ramkrishna Rotake, Shiv Govind Singh *

Department of Electrical Engineering, Indian Institute of Technology, Hyderabad, Telangana, 502285, India

ARTICLE INFO

Keywords:
Biomarker
SnS_2-CNT Composite
Chemiresistive biosensor
Machine learning
Feature importance
ML Explainability

ABSTRACT

The high worldwide mortality and disproportionate impact of cardiovascular diseases have emerged as the most significant global health burden, unfortunately, unmet by the traditional detection methods. Therefore, developing a rapid, sensitive, selective, and rugged biosensor for the precise classification/quantification of cardiac biomarkers is a stepping stone for the future generation of cardiac healthcare. We demonstrate a facile, time-efficient, and scalable biosensor for classifying the FDI approved gold standard cardiac biomarker Troponin-I (cTnI) in untreated human serum matrix, built-on 2-D SnS_2 and 1-D MWCNT composite transducer and decision-tree based explainable machine learning (ML) algorithm. The proposed methodology is further enhanced using an inimitable Operating-Voltage-Selection-Algorithm (OVSA), which boosts ML accuracy to ~100%. The near-perfect classification is realized by strategically incorporating this two-step algorithm-first the OVSA, then the heuristic and ML approaches on the selected dataset. Dynamic concentrations of the biomarker (100 fg/mL to 100 ng/mL) are estimated with high sensitivity, ~71 $(\Delta R/R)\ (ng/mL)^{-1}cm^{-2}$ and low limit of detection (0.02 fg/mL), aiding to the prediction and prognosis of acute myocardial infarction. The hyper-parameter tuning and feature engineering improve the decision process of the ML algorithm, fostering robustness against data variability. Feature importance indices, namely the Gini index, Permutation Importance, and SHAP values, portray 'Voltage' as the most important feature, further justifying our insight into the OVSA. The biosensor's specificity, selectivity, reproducibility and stability are effectively demonstrated with the sampling to result reporting time of just 20 min, establishing it as a potential candidate for clinical testing.

1. Introduction

The early diagnosis of acute myocardial infarction (AMI) carries a substantial potential for life-saving and life-extending experiences (Amsterdam et al., 2014). As per the recommendation of the American Heart Association, apt detection of cardiac biomarkers from the complex biological fluid with a preferred turnaround time (~30 min) is crucial for deciding the optimal treatment strategies in the emergency department (ED) (Benjamin et al., 2019). Among the biomarkers, cardiac troponin-I (cTnI), approved by FDI is very specific to AMI and regarded as the gold standard for detecting myocardial injury (Zhao et al., 2021). The trend of cTnI concentrations after patient admission at ED (0, 30, 60, and 90 min) is valuable for accurate diagnosis (Ng et al., 2001). Additionally, serial monitoring of the biomarker level is recommended for the short and long-term prognosis, adding valued information to heart health (Ouyang et al., 2021a). But the central laboratory-based traditional detection methods have posed limitations in affordable and equitable healthcare services, thereby restraining the point-of-care cardiac diagnosis. The heavy and costly instrumentations need for trained human resources, relatively long sample processing time, and substantial duration from sample collection to result have been some of such systems' significant bottlenecks (Supraja et al., 2021). Even ECG sensitivity may be low (~50%), and in non-ST-segment elevated AMI, it poses a very high risk leaving no other way but biomarker identification for correct diagnosis (Liu et al., 2016). Further, the deadliest outburst of the Covid-19 pandemic and associated cardiac complexity has necessitated a facile, sensitive, portable, and cost-effective biosensor urgently (Rusu et al., 2022).

The endeavour to realize such a biosensor has eventually led to the development of sensor technologies like enzyme-linked immunosorbent

* Corresponding author.
E-mail address: sgsingh@ee.iith.ac.in (S.G. Singh).

https://doi.org/10.1016/j.bios.2022.114915
Received 17 September 2022; Received in revised form 3 November 2022; Accepted 12 November 2022
Available online 14 November 2022

assay (ELISA) (Chin et al., 2020), electrochemiluminescence (ECL) (Du et al., 2020), surface plasmon resonance (SPR) (G. Wang et al., 2022), microcantilevers (Lei et al., 2021), etc., yet seldom meeting the demands of the state-of-the-art necessities. Challenges like quantifying an extensive range of target concentrations, achieving a very low LOD, and eliminating interfering effects still perturb the sensor performance. Recent advances in label-free detection techniques open up a new horizon in the electrochemical (Jo et al., 2015), piezoelectric (Pohanka, 2018), and field-effect transistor (FET) (Wang et al., 2021) based biosensor devices, thereby encouraging revolutionary outcomes in the point-of-care biosensing technology. But, to prove their pertinence in a nonhospital setting ubiquitously, issues like robustness, large-scale manufacturability, and cost-effectiveness still need improvement (Liu and Yobas, 2014)' (Hakim et al., 2012).

The electrical signal-based label-free biosensors got paramount attention for their vast sensing options in various analyte detection assays (So et al., 2021). The flexibility in signal acquisitions, nano to micro-scale of sensor arrays, high sensitivity to target analytes, excellent resolution, compatibility with large-scale semiconductor processing, and real-time label-free detection in the nascent form of the bio-analyte renders them profound importance (Qian and Wang, 2010). These biosensors analyze the target analyte by monitoring different electrical parameters responding to a triggering potential or current signal (Huang et al., 2020)' (Shen et al., 2019)' (Liu et al., 2016). Such chemiresistive devices consist of interdigitated electrodes (IDE) fingers with opposite polarities, separated by a specific gap size and often integrated with nanomaterials as a transducing element that provides the necessary functionalization. The surface potential profile changes upon immobilization of the bio-analyte, thereby modifying the electrical parameters, which would eventually be reflected in the IV characteristics (Chandran et al., 2017)' (Choi et al., 2010). The platform's sensitivity improves due to the synergetic effect of the nanomaterials with the analyte (Holzinger et al., 2017)' (Bolotsky et al., 2019). This approach has successfully detected an enormous variety of targets such as DNAs(Thiha et al., 2018)' (Tripathy et al., 2021), antigen-antibody (Supraja et al., 2021), gas sensing (Naganaboina and Singh, 2022), small molecule detection (Cella et al., 2010) etc.

Generally, metal oxides (e.g., ZnO, TiO_2, CeO_2, etc.), metal sulfides (e.g., MoS_2, etc.), carbon-based nanomaterials like CNTs, Graphene, conducting polymers, etc. are most widely used in biosensors, following two distinct strategies (Jacobs et al., 2010). Firstly, it should possess a high specific surface area for enhanced loading of biochemicals to realize the probe immobilization. Secondly, the nanomaterial should be sufficiently conducting for electrical signal acquisition between two otherwise insulated fingers of IDEs (Zhao et al., 2021). Tin disulfide, SnS_2, a 2-D layered semiconductor with bandgap 2.2–2.4 eV, is an attractive material due to its exciting electrical and optical properties. Owing to its high specific surface area and carrier mobility, good oxidative and thermal stability, etc. SnS_2 has widely been used in gas sensing, photovoltaics, and optoelectronic devices (Shown et al., n.d.)' (Liu et al., 2019)' (Burton et al., 2016). But very few biosensors have been constructed with SnS_2, and due to its near insulator behaviour, there has been no evidence of its application in chemiresistive sensing (Goswami et al., 2022)' (Li et al., 2013).

In light of the above discussion, we have hydrothermally synthesized an SnS_2-MWCNT composite (SnS_2: matrix, MWCNT: filler) to construct a chemiresistive biosensor (Fig. 1B). Unlike many pristine metal oxides and sulfides, the composite shows Ohmic IV characteristics reducing the inherent error in calculating the resistance of the device, which would otherwise negatively impact the repeatability and reproducibility (Tripathy et al., 2019). However, on exposure to the bio-analytes, a more complicated functional relationship is observed between voltage and current, demanding the need for higher-order polynomials for the sensor characteristics (So et al., 2021)' (J. Wang et al., 2022). Therefore, we have proposed a unique Operating-Voltage-Selection-Algorithm (OVSA), to choose a suitable voltage range for the sensor operation.

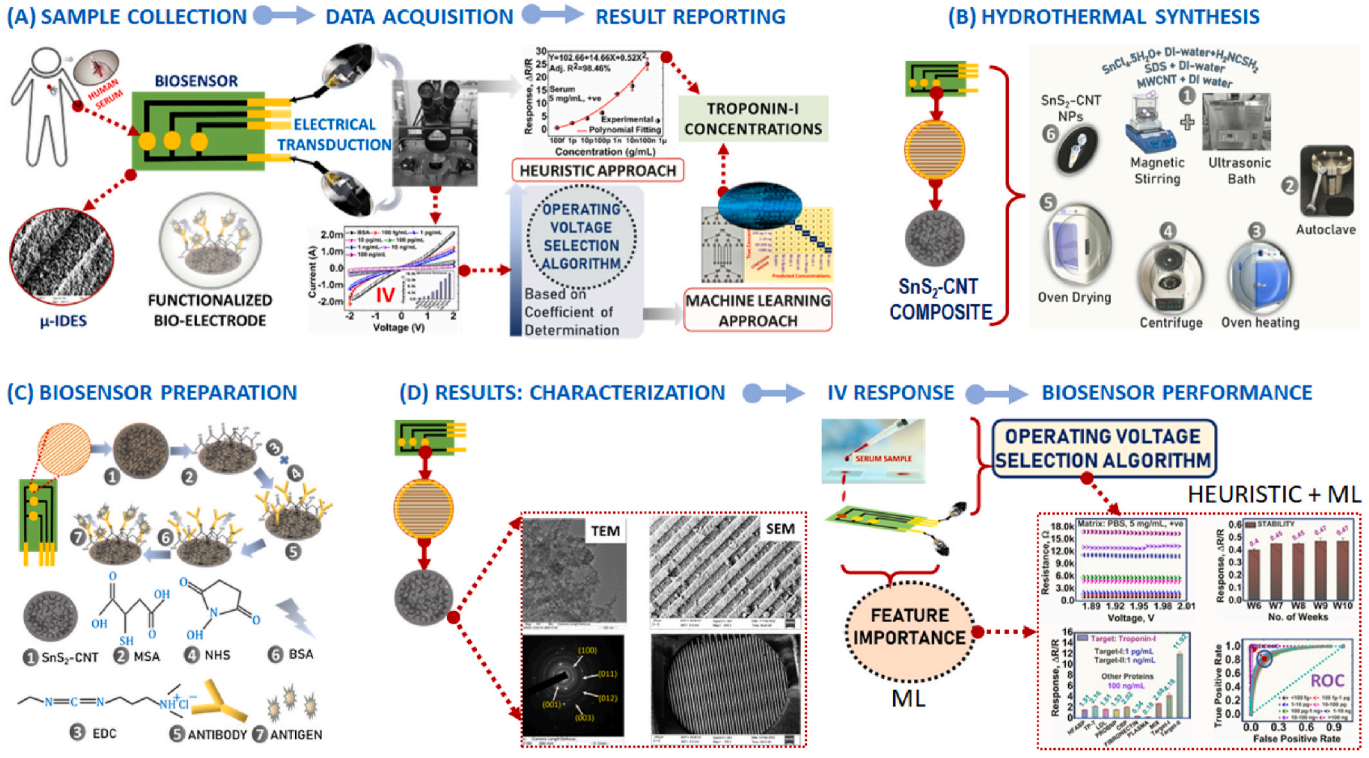

Fig. 1. Schematic representation of the methodical work-flow of the paper. (A) Step-by-step methodology of the research-work from sample collection through data acquisition till the reporting of results, (B) Process steps for the hydrothermal synthesis of SnS_2-CNT composite nanomaterial, (C) Biosensor preparation protocol by functionalizing the interdigitated microelectrodes, (D) Characterization of the synthesized composite and biosensor, IV response and performance evaluation of the biosensor.

Based on the coefficient of determination, the algorithm adequately improves data processing and visualization of the biosensor characteristics. Again, machine learning (ML) models are incorporated to analyze sensor datasets for their strong predictive power, better accuracy, and robustness to noise (Zhang et al., 2021)' (Alam et al., 2019). Through the rigorous model optimization, feature engineering, and hyperparameter tuning along with the OVSA, the ML model's accuracy got improved from ~21 to 78%, and AUC improved from ~63 to 96% for the worst case and to ~100% in the best case. Towards explainability of the ML model, feature importance in the random forest algorithm is studied with three indices: Gini index, Permutation Importance, and SHAP values, where 'voltage' turns out to be the most noteworthy feature. Thus, our approach for the OVSA gets further augmented with the ML results, where both strategies work in tandem to improve the overall accuracy of the proposed biosensor. To the best of our knowledge, this is the first demonstration of a two-step algorithm for improving classification accuracy both in the heuristic and ML approaches. The biosensor has been benchmarked for the vital performance parameters and turnaround time, establishing its added value in this context vis the existing evidence (A-V, Table-S6 of the Supplementary Material). Furthermore, the device's sensitivity, selectivity, interference, stability, repeatability, and reproducibility are examined. Thus, we have developed a time-efficient, and portable biosensor for detecting cTNI with high repeatability (Total ñ350), which carries substantial potential for clinical diagnostics. Additionally, further improvement towards portability of the biosensor platform paves the way for the early detection of the target biomarker and opens up a new window for near future commercialization.

2. Material and methods

2.1. Material

The details of the chemicals and reagents have been discussed in A-I of the Supplementary Material.

2.2. Methods

2.2.1. Synthesis of SnS_2-MWCNT composite

The SnS_2-CNT composite was synthesized using a surfactant-modified mild hydrothermal method with a slight modification of the protocol reported in our previous work (Goswami et al., 2022). Briefly, 27 mM (500 mg) SDS was mixed in 64 mL of DI water followed by 20 min of magnetic beads stirring. Subsequently, 17 mM (378 mg) tin chloride pent hydrate ($SnCl_4.5H_2O$) and 62 mM (300 mg) thiourea (H_2NCSH_2) were added to the former mixture and the solution was subjected to 20 min of stirring. Thereafter, 0.5 wt% MWCNT is added to the mixture and is ultrasonicated for 1 h. The resultant mixture was transferred to a Teflon-lined stainless-steel autoclave and heated at 180 °C for 12 h. The precipitate was collected and washed with DI water, ethanol, and acetone. After heating at 60 °C for 2 h, the bronze-yellow-blackish powder of the composite had been collected.

2.2.2. Bioelectrode preparation

As depicted in Fig. 1C, 1.5 μL of the nanomaterial solution (composite-DMF dispersion) was dropped cast onto each chemiresistive sensor device at three steps (0.5 μL x 3). The sensors were then dried in the oven at 37 °C, and treated with 1.5 μL of 10 mM MSA-DI water mixture. A self-assembled monolayer (SAM) got formed via thiol chemistry (Goswami et al., 2022). Following that, 1.5 μL each of 0.4 M EDC and NHS solution was added sequentially on top of the sensor devices, maintaining 2.5 h interval. The EDC-NHS crosslinking chemistry activated the functionality of the carboxylic groups (Wang et al., 2021). Subsequently, 1.5 μL of troponin-I antibody probe (1 μg/mL in 0.1 M PBS; pH = 7.4) specific to human cTnI protein (target) was introduced into the functionalized sensor surface. The devices were then stored in 4 °C for 12 h so that the antibodies are covalently bonded via the formation of a peptide bond (–CO–NH bond). To block the non-bonded surface groups, the devices were treated with an appropriate mixture of BSA in PBS and incubated at 37 °C (Supraja et al., 2021)' (Tripathy et al., 2021)' (Goswami et al., 2022). Subsequently, the sensors were washed with PBS buffer to avoid any unwanted substances on the sensor surface.

2.2.3. Biosensor response

Towards the detection of the target, the sensor was exposed to different concentrations of cTnI protein aliquots (1.5 μL volume) in PBS buffer and untreated human serum, and thereafter incubated at 37 °C for 15 min. Subsequently, it was washed with PBS and dried, and then the response was recorded using the Probe station (Fig. 1A). Both the heuristic and ML approach were used for the calibration of sensor response. For the preparation of the calibration curves, the voltage range for device operation is selected using an Operating-Voltage-Selection-Algorithm discussed in details in the A-III of the Supplementary Material. The sensor performance parameters, namely, sensitivity, are calculated as slope/area, where 'slope' represents the slope of the calibration curve, and 'area' represents the active working area of the device. The LOD has been calculated by using the 3σ method. The details of the interference, selectivity, reproducibility and stability studies are presented in the 'Results and Discussion' section. Notably, here we've tested only one concentration of the target analyte per device to resemble closer proximity towards the clinical scenario.

3. Results and discussion

3.1. Material characterization

The SnS2-MWCNT composite was characterized thoroughly to confirm its crystal structure, elemental composition, and morphology with X-Ray Diffraction (XRD), X-Ray Photoelectron Spectroscopy (XPS), Transmission Electron Microscopy (TEM), and Scanning Electron Microscopy (SEM) and the results are presented in Fig. 2. Specifically, Table-S1 and Table-S2 of the Supplementary Material presents the details of the comparative studies between the pristine SnS_2 and the SnS2-MWCNT composite in terms of interplanar distance, average crystallite size and the microstrain consulting XRD data. The detailed discussion has been performed in the A-II of the Supplementary Material.

3.2. I–V characteristic of the composite

The electrical characteristics of the pristine SnS_2 and the composite were evaluated in ambient conditions with an Agilent B1500A semiconductor device analyzer in conjugation with a Cascade Microtech probe station. The nanomaterial forms a continuous network between the IDE fingers to establish a semi-conducting pathway, which was insulated otherwise (inset of Fig. 2.D.1). This network is precisely equivalent to a parallel and series combination of R's and C's between the fingers of μ-IDEs, constituting numerous pathways for charge transport (Tripathy and Singh, 2021). The carriers follow the law of minimum action and hence always prefer to choose the lowest impedance path (Madriz et al., 2009). The conduction of the charge carriers is temperature-dependent and governed by various mechanisms signified by the temperature-conductivity relation. In particular, intrinsic excitation, trap activation, nearest-neighbor hopping, variable range hopping, interfiber tunneling, etc., are some of the mechanisms inherent to these nanomaterials (Zubair Ansari and Khare, 2015)' (Kim et al., 2018). Notably, the electron affinity of SnS_2 χ_{SnS2} is known to be 4.2 eV with a bandgap of 2.18–2.44 eV. Ultimately, $\Phi_{SnS2} = \chi_{SnS2} + (E_c\text{-}E_f) \cong$ 5.29–5.42 eV, larger than that of the work function of gold, 4.83 eV (Voznyi et al., 2016). Since the contact metal work function is lower than that of the SnS_2, an n-type semiconductor, a non-rectifying contact is established.

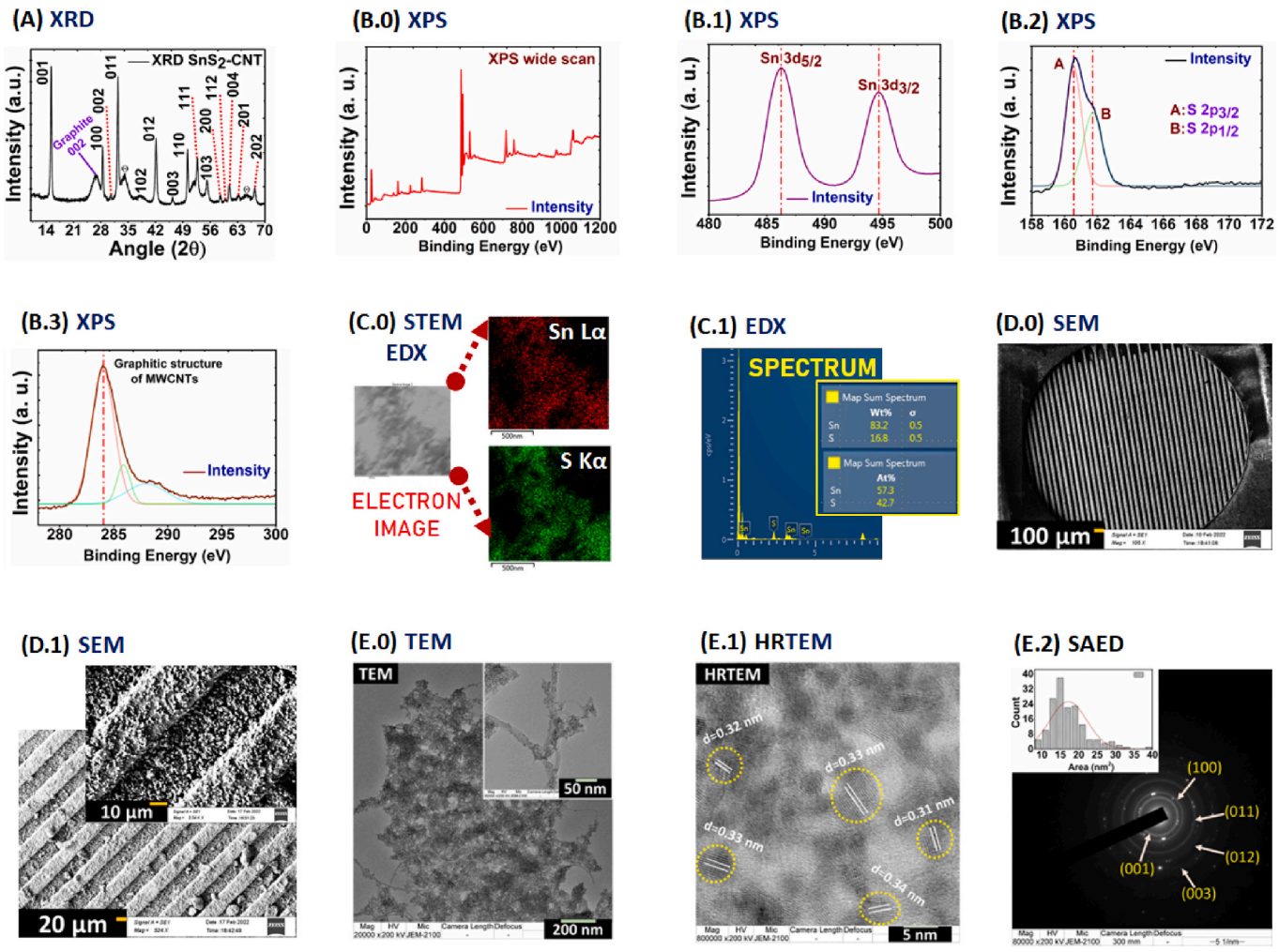

Fig. 2. Characterization (A) X-ray diffraction (XRD) elucidating the indices of the crystal planes (B.0) X-ray Photoelectron spectroscopy (XPS) showing the wide scan of binding energies versus intensity, (B.1) XPS narrow scanning spectrum depicting binding energies for Sn 3d orbitals, (B.2) XPS narrow scanning spectrum depicting binding energies for S 2p orbitals, (B.3) XPS narrow scanning spectrum depicting binding energies for MWCNTs, (C.0) STEM mode electron image of SnS_2-CNT composite nanomaterial, EDAX mapping image of the composite showing the distribution of Sn and S elements, (C.1) EDAX spectrum describing the peaks corresponding to the constituent Sn and S atoms (D.0) SEM image showing the active area of a chemiresistive device, (D.1) SEM image of the µIDEs after drop cast of the nanomaterial on the chemiresistive device, inset shows a higher resolution SEM image showing nanomaterial particles distribution between two fingers of a chemiresistive device (E.0) TEM image of the SnS_2-CNT nanocomposite showing the fine grains of embedded SnS_2 nanoparticles in nanometre-range and long CNT fibres, inset shows a magnified image, (E.1) HRTEM image of the composite showing lattice fringes, d spacings of a few planes are marked in the image, (E.2) SAED pattern from the nanocrystals of SnS_2-CNT composite with the indexed rings, inset shows the distribution of particles from TEM image E.0.

Although the pristine SnS_2 nanomaterial is very promising for the biosensor application for its good surface adhesion behaviour, high specific surface area, facile realization of bio-conjugation via thiol chemistry, good electrical contact with the metal electrodes etc., yet there exist some burning challenges (Goswami et al., 2022) (Yuan et al., 2017). The primary concern regarding the I–V characteristic of intrinsic SnS_2 nanomaterial (A-I, Supplementary Material) is its feeble current response (Fig. 3A,B), thereby limiting the transduction capability. However, the composite nanomaterial, prepared by doping SnS_2 with 0.5 wt% of MWCNTs, overcomes this challenge without affecting the merits of its pristine counterpart. The devices (n = 10) decorated with the composite showed near Ohmic behaviour for a sizeable potential range of −10 to 10 V (Fig. 3E). The experimental data were fitted with linear curves ($y = a + bx$) in Fig. 3F and Fig. 3G for the voltage ranges from 0 to 10 V (Quadrant-I) and −10 to 0 V (Quadrant-III). Interestingly, the slope of the fitted curves remained unchanged (0.007 units), confirming the non-rectifying contact between the composite nanomaterial and metal electrodes. There is no power-law relation between the current and voltage for the composite, unlike pristine SnS_2(Voznyi et al., 2016). Again, the log-log plot between I–V in Fig. 3H excludes any possibility of slope transition of the I–V characteristic, i.e., IαV persists. Therefore, unlike the pristine SnS_2, in the composite material, no signature of trap-mediated SCLC was found from the I–V characteristic' (Rose, 1955).

It is worth noting that, the inter-device variability had been a well-pronounced phenomenon in the biosensor domain. Owing to the randomness of the manual operations inherent to the sensor development protocol, the devices show a variable response (Goswami et al., 2022)' (Tripathy et al., 2019). The non-Ohmic behaviour of the transducing material complicates the situation further by contributing to the device variability. Fortunately, the linear I–V response of the composite aids in the mitigation of device variability to a substantial extent. Fig. 3I depicts the resistances of 10 devices, the error bars show the spread in resistance, and % RSD lies below 10. Again, to estimate the impact of the distribution of the composite on device performance, three different composite-DMF dispersions (10, 5, and 1 mg/mL) were cast on the devices. From the I–V characteristics of Fig. 3J, it is evident that with a decrease in the nanomaterial concentration, the current reduces, but the

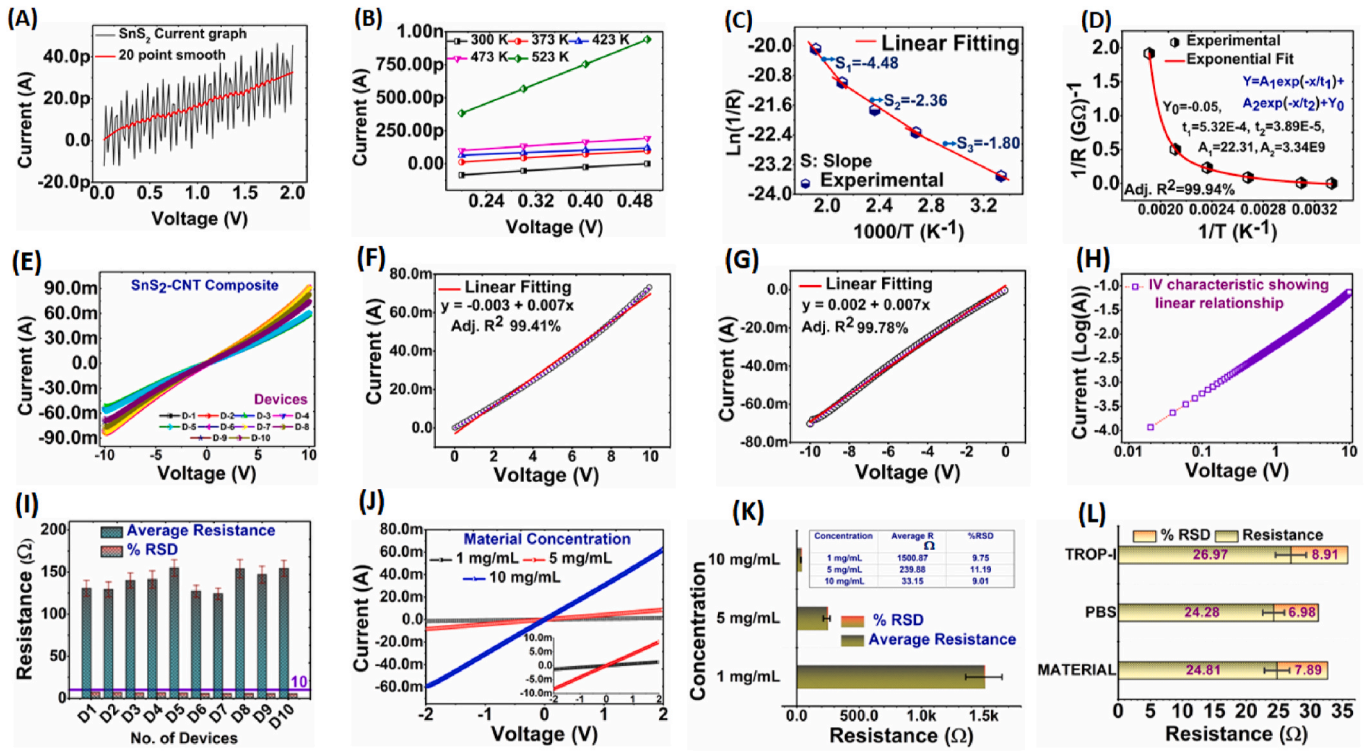

Fig. 3. (A) Current-voltage characteristic of SnS_2 nanoparticles representing near-insulator behaviour, (B) Current-voltage characteristic of SnS_2 with a variation of temperature, (C) Arrhenius plot of SnS_2 nanoparticles, (D) Conductance-temperature dependence of the SnS_2 nanoparticles, (E) Near Ohmic current-voltage characteristic of SnS_2-CNT nanocomposite material in a large voltage range of −10 to 10 V, (F) Linear fitting of IV characteristic in the potential range of 0–10 V, (G) Linear fitting of IV characteristic in the potential range of −10 to 0 V. (H) Log-Log plot of current versus voltage showing linear relation, (I) % R.S.D. and average resistance response of 10 identical devices, resistance averaged over −10 to 10 V, (J) Linear IV characteristic for different dilutions of SnS2-CNT composite in D.M.F. solvent in a voltage range of −2 to 2 V showing an averaged current value of 10 devices at each nanomaterial concentration, (K) % R.S.D. and average resistance of 10 devices each for three concentrations of the nanocomposite dispersed in D.M.F. solvent, (L) Resistance and % R.S.D. value of 10 devices incubated with different interfering agents without any chemical immobilization, showing minimal deviation.

linearity persists. The average resistances of 10 devices of each material concentration along with the % RSD is tabulated at the inset of Fig. 3K. When the nanomaterial concentration was decreased (10-1 mg/mL) by keeping the same drop cast volume ($0.5 \times 3 = 1.5$ μL), the number of particles between two metallic fingers decreased; hence the corresponding increment of resistance was observed. Furthermore, to envisage the importance of functionalization protocol (Fig. 1C), the nanomaterial decorated electrodes were directly exposed to the target protein (troponin-I) and PBS matrix. The recorded resistances with the % RSD ($n = 6$) are reported in Fig. 3.L depicting minimal change in resistance on incubation with target chemicals. This is because the proteins would not directly bind to the nanomaterial without immobilizing the functional biochemicals, and no transduction was achieved (Prakash et al., 2016).

3.3. *I–V response of the cTnI biosensor*

If cTn levels increase beyond the 99th percentile of the upper reference limit, myocardial injury is detected (medical cut-off ~40 pg/mL) (Ouyang et al., 2021b)' (Wang et al., 2021). Therefore, quantifying cTnI concentrations and recognizing its changing pattern is vital for diagnosis and prognosis of AMI. Here, we have classified cTnI concentrations through a bioelectronic platform based on the antigen-antibody interaction, where the monoclonal antibody is covalently immobilized on the bioelectrode. The human body fluid, i.e., whole blood, plasma, serum has a pH value of 7.35–7.45. Whereas, in the human body, the antigen-antibody reactions occur at a body fluid temperature of 37 °C. To replicate a similar environment, untreated human serum was taken and PBS matrix with pH 7.4 was chosen for the control experiments (Jo et al., 2015)' (Liu and Yobas, 2014).

Interestingly, after the immobilization of the biochemicals, the I–V characteristics are not purely Ohmic (Fig. 4A and B). Consequently, R keeps changing with the voltage sweep. Again, on further exposure to target protein concentrations, it shows a complex functional relationship (IαV does not hold). Hence, it becomes crucial to define suitable voltage ranges for calculating the resistances and thereby sensor response, but the exact scheme was missing (Bhattacharyya et al., 2011)' (García-Aljaro et al., 2010). To overcome such an issue, we've developed the OVSA, based on the coefficient of determination. Hence, resistance, the primary parameter for biosensor calibration, was calculated with a minimal error by narrowing down the voltage window (A-III, Supplementary Material). Thus, after the probe immobilization, the resistance values of 10 devices illustrated the repeatability of the biosensor (inset of Fig. 4A).

As the antigen-antibody interaction occurs at the surface of the bioelectrode, the surface properties of the nanomaterial change, thereby affecting the charge transport. This may arise regarding the alteration of surface charge, surface potential, etc., ultimately leading to the modification in the transport characteristics (Stafiniak et al., 2011)' (Cui et al., 2001). Specifically, the surface charge in BSA and the cTnI protein fractions is negative at the working pH, 7.4, since their pI values are around ~5 (Peronnet et al., 2007)' (Martucci et al., 2020). Therefore, as more and more antigen concentrations are fed into the biosensor, more surface areas get occupied by the antigen-antibody complex, and the surface charge becomes increasingly accumulated. Therefore, the impact of the complex would be more pronounced with higher antigen concentrations, thereby increasing the resistance values (inset of Fig. 4B) (Supraja et al., 2021)' (He et al., 2007). In principle, these piled

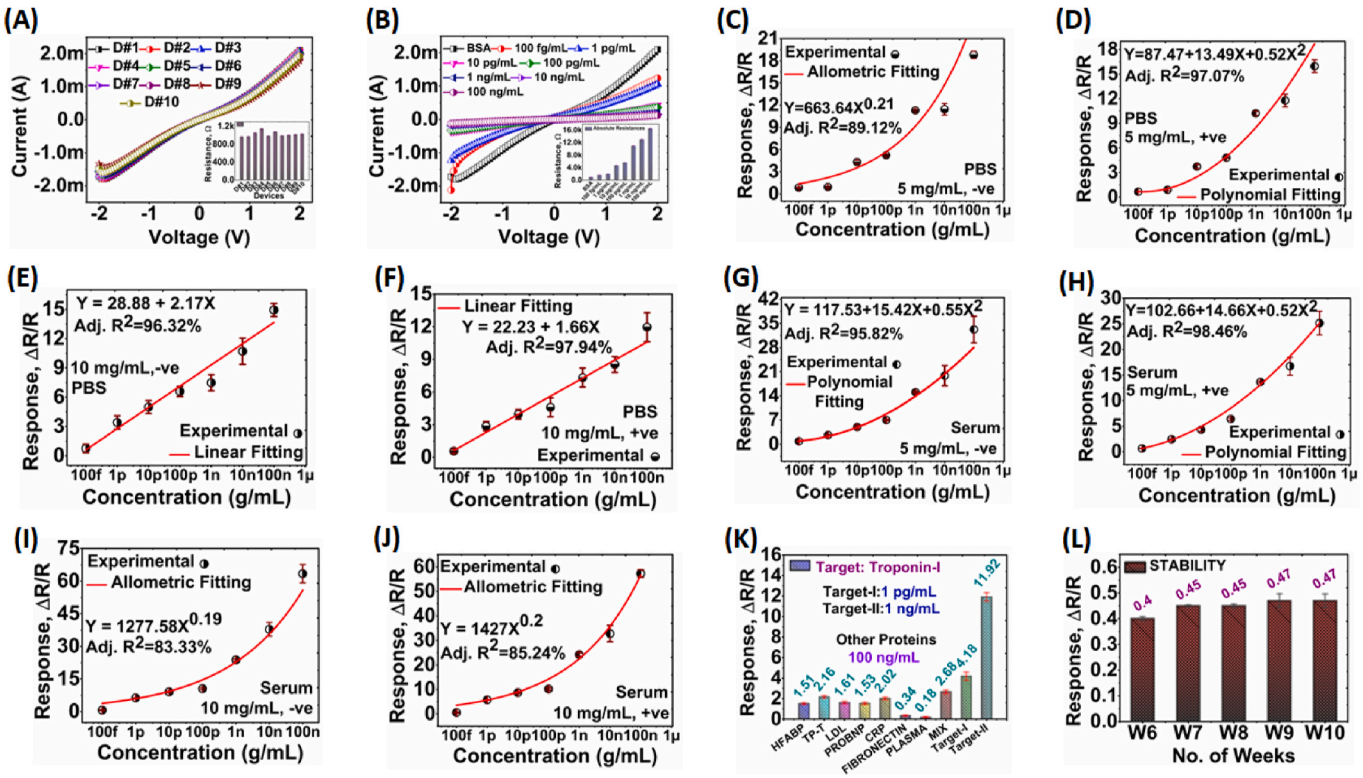

Fig. 4. (A) I–V characteristic of 10 devices after incubating with B.S.A., inset shows the resistance of each device (B) I–V characteristic of a biosensor at each step of incubation with target concentrations from 100 fg/mL to 100 ng/mL, inset shows the resistance for each incubation step (C) Calibration curve of the biosensor; 5 mg/mL composite-DMF dispersion,-ve voltage polarity, Matrix: PBS, (D) Calibration curve of the biosensor; 5 mg/mL composite-DMF dispersion,+ve voltage polarity, Matrix: PBS, (E) Calibration curve of the biosensor; 10 mg/mL composite-DMF dispersion,-ve voltage polarity, Matrix: PBS, (F) Calibration curve of the biosensor; 10 mg/mL composite-DMF dispersion,+ve voltage polarity, Matrix: PBS, (G) Calibration curve of the biosensor; 5 mg/mL composite-DMF dispersion,-ve voltage polarity, Matrix: Serum, (H) Calibration curve of the biosensor; 5 mg/mL composite-DMF dispersion,+ve voltage polarity, Matrix: Serum, (I) Calibration curve of the biosensor; 10 mg/mL composite-DMF dispersion,-ve voltage polarity, Matrix: Serum, (J) Calibration curve of the biosensor; 10 mg/mL composite-DMF dispersion,+ve voltage polarity, Matrix: Serum, (K) Interference and selectivity studies with non-target proteins, viz. HFABP, Troponin-T (TP-T), LDL, ProBNP, C.R.P., FIBRONECTIN, PLASMA and mixture of them all, respective concentrations are noted in the legend (L) Stability study of the probe for 10 weeks of storage duration, showing minimal deviation in ΔR/R response.

up charges would affect the transport of the injected carriers within the nanomaterial network, behaving similarly to the V_T shift due to DNA hybridization reported elsewhere (Boileau et al., 2019).

3.4. Calibration of the biosensor

The functional relationship of the biosensor response with the target analyte concentrations is illustrated with calibration curves considering both voltage polarities. The calibration curve obtained for a voltage range of −2 to 0 V was denoted with '-ve,' and that for 0–2 V was marked with '+ve' in Fig. 4. (C–K). Furthermore, separate calibration equations were obtained to highlight the matrix effect (PBS and serum). The experimental data selected for the calibration by the OVSA were fitted with three mathematical functions: linear ($y = mx + c$), allometric ($y = ax^b$), and polynomial ($y = a + bx + cx^2$) (Fig. 4).

In all the calibration curves, an increasing pattern of sensor response is observed with the addition of target concentrations. The influence of matrix (blank test), calculation of LOD by 3σ method), and the sensor's sensitivity are presented illustratively in the A-III (Table-S3) of Supplementary Material. The augmented biosensor performance in terms of sensitivity, selectivity and LOD can be attributed to the efficient synthesis and electrical performance of the composite nanomaterial, mature development of the bio immobilization protocol via covalent antibody-surface binding, monoclonal antibody mediated antigen-antibody interaction and finally the effective transduction mechanism. However, it was observed that the calibration equation could not fit the experimental results with 100% accuracy and the experimental data points deviate significantly from the fitted curve. The adjusted R^2, implicating the goodness of fit of the mathematical equations, varies between 83.33% and 98.43%. This deviation, pertaining to the modification in experimental conditions, may arise due to variation in the extent of functionalization and the inherent variability of the antigen-antibody complex formation process (Tripathy et al., 2019)' (Reverberi and Reverberi, 2007). This behaviour demands the application of advanced techniques like machine learning algorithms (MLAs) to estimate target analyte concentrations accurately, discussed further in the manuscript.

3.5. Interference, selectivity, and stability studies

The target biomarker is embedded in a complex matrix of other non-specific proteins and biological compounds in the clinical environment. Hence, to realize the practical applicability of the biosensor in a clinical setting, we have examined the cross selectivity and interference in the human serum matrix (Goswami et al., 2022). A known high concentration (100 ng/mL) of non-target proteins (as mentioned in Fig. 4K) was drop cast (1.5 μL in volume) onto the sensor surface, first individually one by one, and finally, a mixture of all of them and the sensor response had been recorded. Subsequently 1 pg/mL (100000X lesser) and 1 ng/mL (100X lesser) concentrations of the target protein was added to the biosensor. The experimental data revealed that with the specific protein being incorporated, the sensor response was 155.97% (target = 1 pg/mL) and 444.77% (target = 1 ng/mL), more than that of the interfering mixture. These results confirm the high specificity of the

biosensor towards the target protein (troponin-I). For the stability analysis, the prepared bioelectrode was stored in the refrigerator (4 °C) in open condition without any packing for several weeks, and corresponding I–V characteristic was recorded each week. As evident from Fig. 4.L, after the end of the 10th week, the ΔR/R for the probe was found to be 0.47. This implies a quite stable behaviour of the biosensor without any degradation upon storage.

3.6. Two-step algorithm for improved classification

Different experimental and statistical approaches have been proposed in the literature to enhance the accuracy, reliability, repeatability, and reproducibility of biosensors (Kim et al., 2021)' (So et al., 2021)' (J. Wang et al., 2022). Yet, there had been some inherent error in the calibration of sensor response with a mathematical function. Herein, we have developed a unique and efficient two-step strategy for optimizing biosensor performance by plugging in the OVSA to curate experimental data and thereby applying ML to the selected dataset (Fig. 5A,B). Typically, in a first principal analysis, Voltage, Normalized Resistance, Normalized Current, V^2/R Normalized Power, and I^2*R Normalized Power were used as the features in ML algorithms. They were sent through various mathematical transforms, finally expanding the feature set from 5 to 21. Then, MLAs were tested with a train test split of 80:20 (Fig. 5. C). Additionally, the K-fold cross-validation was employed to avoid any effect of bias (Acharyya et al., 2020). Finally, the troponin-I concentrations were predicted with the ML model in the form of a confusion matrix, and the receiver operating curve (ROC) was plotted considering the cTnI concentrations (Fig. 5. D).

From the results, it is evident that, unlike the mathematical calibration equations, the ML algorithms are able to predict the troponin-I concentrations with ~100% accuracy. The performance matrices (e.g., accuracy, precision, AUC, F1 score, and recall) associated with the ML algorithms were also evaluated, and a comparison is presented (A-IV, Table-S4 and Table-S5 of the Supplementary Material). We found that Random Forest (RF) Algorithm was the most consistent in giving excellent outputs by mitigating the data variability from different devices. This is because it works on multiple decision trees and provides robustness against the scale of the feature's values. The prediction is based on piecewise constant approximations, further improved by averaging. The hyperparameters, obtained from a grid search algorithm were tuned for each experimental dataset to optimize the algorithm (Kumar et al., 2020). Notably, after incorporating the OVSA, the ROC characteristics improved drastically (Fig. 5. D). Precisely, the AUC values improved from 63 to 96% for the worst case and up to 100% for the best case, demonstrating the algorithm's efficacy.

3.7. Machine learning explainability

Besides the high accuracy, robustness, and outstanding performance of the ML algorithms, the feature importance map provides key insights into the underlying physical phenomena (Z. Wang et al., 2022). Herein, the contribution of each feature towards the RF model was evaluated under three criteria. Firstly, how the model scores the features according to its own scoring criterion, evaluated by Gini index (Pedregosa et al., 2011). Secondly, how each feature contributes to individual predictions-estimated through the mean of Shapley additive explanations (SHAP). At last, what is each feature's contribution toward each class-determined via the Permutation Importance and Partial Dependence Plots. Addressing these criterions aids greatly to the explainability of the model and help weed out redundant features that negatively contribute to the model accuracy (Fig. 6). Permutation importance tells us the effect on model accuracy if the data in a particular column has been shuffled. The Partial dependence plots helped us visualize the importance of features in predicting each class. It was seen that some features have a higher value in a particular class. For example, it can be seen that the I^2R values give us good information gain in the lower

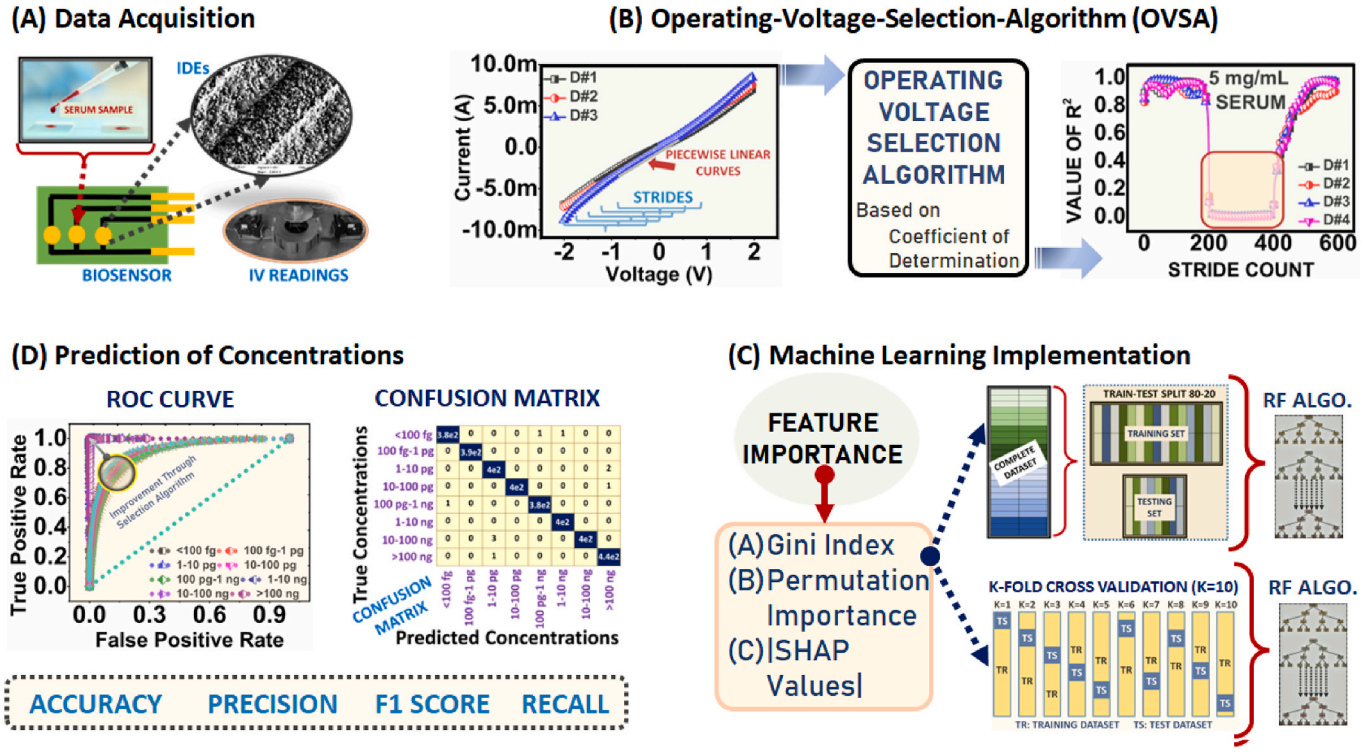

Fig. 5. Machine Learning strategies for enhancing classification accuracy and better predictions of the analyte concentrations. (A) Schematic representation of the sample testing and data acquisition. (B) Operating-Voltage-Selection-Algorithm based on coefficient of determination. (C) Implementation of machine learning algorithms by train test splitting (80–20) and K-fold cross validation to eliminate bias effect. (D) Predictions of troponin-I concentrations and evaluation of performance matrices of M.L.A.s, confusion matrix and receiver operating characteristic.

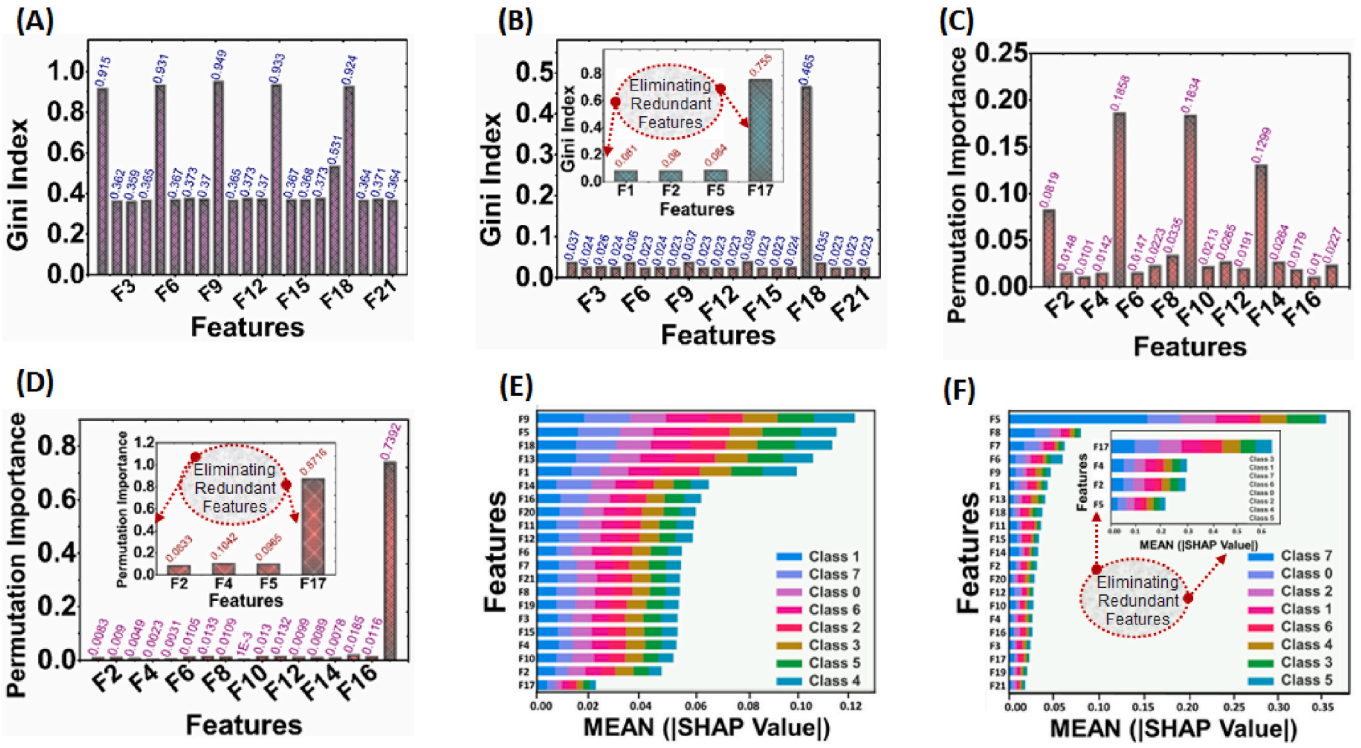

FEATURES: F1: Normalized (I^2R)_Inverse, F2: Normalized (V^2/R)_Inverse, F3: Normalized (I)_Inverse, F4: Normalized (R)_Inverse, F5: Normalized (I^2R)_Yeo Johnson, F6: Normalized (V^2/R)_Yeo Johnson, F7: Normalized (I)_Yeo Johnson, F8: Normalized (R)_Yeo Johnson ,F9: Normalized (I^2R)_Cube, F10: Normalized (V^2/R)_Cube, F11: Normalized (I)_Cube, F12: Normalized (R)_Cube, F13: Normalized (I^2R)_Square, F14: Normalized (V^2/R)_Square, F15: Normalized (I)_Square, F16: Normalized (R)_Square, F17: Voltage (V), F18: Normalized (I^2R), F19: Normalized (V^2/R), F20: Normalized (I), F21: Normalized (R)

(G) Recovery Studies: Prediction Of Classes & Estimation of Concentrations

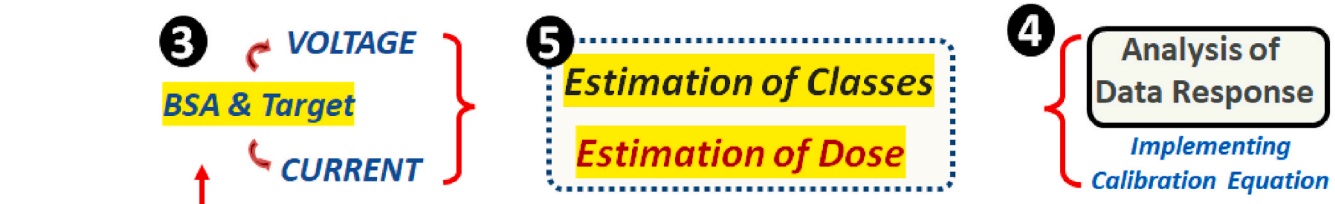

Tested dose (T)	Estimated Dose (E)	Predicted Class	Error[(T-E)/T]
350 fg	227 fg	100 fg – 1 pg	0.348
6 pg	3.67 pg	1-10 pg	0.388
75 pg	55 pg	10-100 pg	0.264
550 pg	387 pg	100 pg – 1 ng	0.295
4.5 ng	2.23 ng	1-10 ng	0.502
75 ng	45.7 ng	10-100 ng	0.390

Fig. 6. Feature importance plots for visualizing the importance of features on the Random Forest Algorithm. Gini Index (A) for the complete dataset. (B) for the *selected dataset, inset shows the performance after eliminating redundant features. Permutation Importance plot (C) for the complete dataset (D) for the *selected dataset, inset shows the performance after eliminating redundant features. Impact of features for classification based on the |SHAP value|(E) for complete dataset. (F) for the *selected dataset, inset shows the performance after eliminating redundant features. Here class 1–7 means the concentration ranges of cTnI from 100 fg/mL to 100 ng/mL *Selected dataset: This dataset had been selected based on the selection algorithm discussed in the manuscript. (G) Cross validation studies towards prediction of classes and dose estimation on random concentration data. Table shows the summary of the results.

ranges, whereas the inverse of voltage gives us a good result in the mid ranges of concentrations. On consulting the complete dataset and linear range obtained from the OVSA using the three-criterion discussed above and subsequently eliminating the redundant features, we derived a set of five features that provide high accuracy and information gain (inset of Fig. 6B,D,F). Upon visualizing a few of the trees in the complete model, it was seen that 'Voltage' was used as deciding feature in the decision tree's upper parts, which implies that it has a significant impact on the decision process and, in turn, the proficiency of RF model.

The explanation for these results can be argued via the conduction mechanism of the nanomaterial network between the IDEs, which is envisaged at two levels i.e., before and after the functionalization. Particularly, the defect states, primarily the trap levels distributed in energy, get activated at certain threshold voltage. Furthermore, when the nanomaterial is functionalized with the biochemicals, the dielectric properties of the network are modified. This in turn affects the spatial distribution of electric field between the μIDEs pertaining to the influence of the local ambiance. The interplay between the accumulated surface charges due to antigen-antibody interaction and the dynamics of the injected carriers are driven by the continuously changing electric field-controlled by the voltage sweep. Therefore, once the suitable voltage range is selected with the OVSA, the most accurate information is obtained to study the biosensor response against the target analyte concentrations. Additionally, it is worth noting that the analytical strategy developed here for evaluating the non-linear I–V characteristic towards sensor performance can be generalized for other electrical signal-based sensing platform.

3.8. Recovery studies for cross validation

To study the model performance on random concentration values and the reproducibility of the experiments, recovery studies are performed. To realize the same, some randomly chosen concentrations were prepared in a pool of untreated human serum and I–V data was acquired. Then from the calibration equation, the dose was estimated using the appropriate root of the quadratic equation, $\text{Predicted Concentration} = -14.66 + \frac{\sqrt{(214.92-4\times0.52\times(102.66-R))}}{(2\times0.52)}$, here R represents response i.e., ΔR/R. For the prediction of the classes, only the BSA and target voltage and current values were fed into the cross-validation process. Notably, 100% accuracy is achieved in classification, and the estimated dose also lies near to the tested values (Fig. 6. G). The results reveal the efficacy of the two-step prediction process developed uniquely in this research-work.

4. Conclusion

In summary, a low-cost, ultrasensitive, and time-efficient Chemiresistive biosensor has been developed here to classify the gold standard AMI biomarker Troponin-I aided with SnS_2-MWCNT composite, ML, and a unique Operating-Voltage-Selection-Algorithm. The Ohmic current-voltage behaviour of the nanomaterial contributes to the mitigation of inter-device variability, thereby enhancing the repeatability and reproducibility of the biosensor. The biosensor performance was evaluated against the target protein concentration (cTn-I, 100 fg/mL to 100 ng/mL; ~3.79 fM to ~3.79 nM) in PBS (pH 7.4) and human serum matrices employing 5 and 10 mg/mL of transducing composite-DMF dispersion. The sensor performance was enhanced by applying ML algorithms with a train test split (80–20), and the bias was checked using K-fold cross-validation. The performance matrices like F1 score, accuracy, AUC, precision, and recall of each of the algorithms had been deducted individually for both cases where the random forest stood out the best. The selectivity, interference, and stability studies were successfully performed, which paved the way for the potential clinical application of the proposed biosensor. Three indices, namely Gini index, Permutation Importance, and SHAP values, were evaluated for feature importance. 'Voltage' turned out to be the most important feature, thereby augmenting the procedure behind the OVSA further and providing adequate explainability to the ML algorithm. Towards the cross validation of the developed methodology, some random concentrations of the target protein aliquots on untreated human serum pool were predicted potentially with the developed model trained with the experimental dataset. In the future scope of this work, developing a portable platform with analyses of clinical samples would render the whole endeavour a successful product for clinical testing.

CRediT authorship contribution statement

Partha Pratim Goswami: Visualization, Methodology, Data curation, Formal analysis, Writing - original draft. **Tushar Deshpande:** Data curation. **Dinesh Ramkrishna Rotake:** Project Administration. **Shiv Govind Singh:** Supervision.

Declaration of competing interest

The authors declare that they have no known competing financial interests or personal relationships that could have appeared to influence the work reported in this paper.

Data availability

Data will be made available on request.

Acknowledgments

We acknowledge the Ministry of Education, Govt. of India, and the Department of Science and Technology for funding this research work. All the device fabrication and characterization facilities like Zeiss Carl EV018 SEM, JEOL JEM 2100 FX TEM, and all other instruments were used with the support of IIT Hyderabad.

Appendix A. Supplementary data

Supplementary data to this article can be found online at https://doi.org/10.1016/j.bios.2022.114915.

References

Acharyya, S., Jana, B., Nag, S., Saha, G., Guha, P.K., 2020. Single resistive sensor for selective detection of multiple VOCs employing SnO2 hollow spheres and machine learning algorithm: a proof of concept. Sensor. Actuator. B Chem. 321 https://doi.org/10.1016/j.snb.2020.128484.

Alam, M.Z., Rahman, M., Saifur, Rahman, Sohel, M., 2019. A Random Forest based predictor for medical data classification using feature ranking. Inform. Med. Unlocked 15. https://doi.org/10.1016/j.imu.2019.100180.

Amsterdam, E.A., Wenger, N.K., Brindis, R.G., Casey, D.E., Ganiats, T.G., Holmes, D.R., Jaffe, A.S., Jneid, H., Kelly, R.F., Kontos, M.C., Levine, G.N., Liebson, P.R., Mukherjee, D., Peterson, E.D., Sabatine, M.S., Smalling, R.W., Zieman, S.J., Anderson, J.L., Halperin, J.L., Albert, N.M., Bozkurt, B., Curtis, L.H., DeMets, D., Fleisher, L.A., Gidding, S., Guyton, R.A., Hochman, J.S., Kovacs, R.J., Ohman, E.M., Pressler, S.J., Sellke, F.W., Shen, W.K., Stevenson, W.G., Wijeysundera, D.N., Yancy, C.W., 2014. 2014 AHA/ACC Guideline for the management of patients with non-st-elevation acute coronary syndromes: executive summary: a report of the American college of cardiology/American heart association task force on practice guidelines. Circulation. https://doi.org/10.1161/CIR.0000000000000133.

Benjamin, E.J., Muntner, P., Alonso, A., Bittencourt, M.S., Callaway, C.W., Carson, A.P., Chamberlain, A.M., Chang, A.R., Cheng, S., Das, S.R., Delling, F.N., Djousse, L., Elkind, M.S.V., Ferguson, J.F., Fornage, M., Jordan, L.C., Khan, S.S., Kissela, B.M., Knutson, K.L., Kwan, T.W., Lackland, D.T., Lewis, T.T., Lichtman, J.H., Longenecker, C.T., Loop, M.S., Lutsey, P.L., Martin, S.S., Matsushita, K., Moran, A.E., Mussolino, M.E., O'Flaherty, M., Pandey, A., Perak, A.M., Rosamond, W.D., Roth, G. A., Sampson, U.K.A., Satou, G.M., Schroeder, E.B., Shah, S.H., Spartano, N.L., Stokes, A., Tirschwell, D.L., Tsao, C.W., Turakhia, M.P., VanWagner, L.B., Wilkins, J. T., Wong, S.S., Virani, S.S., 2019. Heart disease and stroke statistics-2019 update: a report from the American heart association. Circulation 139. https://doi.org/10.1161/CIR.0000000000000659.

Bhattacharyya, D., Senecal, K., Marek, P., Senecal, A., Gleason, K.K., 2011. High surface area flexible chemiresistive biosensor by oxidative chemical vapor deposition. Adv. Funct. Mater. 21 https://doi.org/10.1002/adfm.201101071.

Boileau, N.T., Melville, O.A., Mirka, B., Cranston, R., Lessard, B.H., 2019. P and N type copper phthalocyanines as effective semiconductors in organic thin-film transistor based DNA biosensors at elevated temperatures. RSC Adv. 9 https://doi.org/10.1039/c8ra08829b.

Bolotsky, A., Butler, D., Dong, C., Gerace, K., Glavin, N.R., Muratore, C., Robinson, J.A., Ebrahimi, A., 2019. Two-dimensional materials in biosensing and healthcare: from in vitro diagnostics to optogenetics and beyond. ACS Nano 13. https://doi.org/10.1021/acsnano.9b03632.

Burton, L.A., Whittles, T.J., Hesp, D., Linhart, W.M., Skelton, J.M., Hou, B., Webster, R. F., O'Dowd, G., Reece, C., Cherns, D., Fermin, D.J., Veal, T.D., Dhanak, V.R., Walsh, A., 2016. Electronic and optical properties of single crystal SnS2: an earth-abundant disulfide photocatalyst. J Mater Chem A Mater 4. https://doi.org/10.1039/c5ta08214e.

Cella, L.N., Chen, W., Myung, N.V., Mulchandani, A., 2010. Single-walled carbon nanotube-based chemiresistive affinity biosensors for small molecules: ultrasensitive glucose detection. J. Am. Chem. Soc. 132 https://doi.org/10.1021/ja100503b.

Chandran, G.T., Li, X., Ogata, A., Penner, R.M., 2017. Electrically transduced sensors based on nanomaterials. Anal. Chem. 2012–2016. https://doi.org/10.1021/acs.analchem.6b04687.

Chin, L.K., Son, T., Hong, J.S., Liu, A.Q., Skog, J., Castro, C.M., Weissleder, R., Lee, H., Im, H., 2020. Plasmonic sensors for extracellular vesicle analysis: from scientific development to translational research. ACS Nano. https://doi.org/10.1021/acsnano.0c07581.

Choi, Jaewon, Lee, J., Choi, Jinsub, Jung, D., Shim, S.E., 2010. Electrospun PEDOT:PSS/PVP nanofibers as the chemiresistor in chemical vapour sensing. Synth. Met. 160 https://doi.org/10.1016/j.synthmet.2010.04.021.

Cui, Y., Wei, Q., Park, H., Lieber, C.M., 2001. Nanowire nanosensors for highly sensitive and selective detection of biological and chemical species. Science 293. https://doi.org/10.1126/science.1062711, 1979.

Du, D., Shu, J., Guo, M., Haghighatbin, M.A., Yang, D., Bian, Z., Cui, H., 2020. Potential-resolved differential electrochemiluminescence immunosensor for cardiac troponin i based on MOF-5-wrapped CdS quantum dot nanoluminophores. Anal. Chem. 92 https://doi.org/10.1021/acs.analchem.0c03131.

García-Aljaro, C., Bangar, M.A., Baldrich, E., Muñoz, F.J., Mulchandani, A., 2010. Conducting polymer nanowire-based chemiresistive biosensor for the detection of bacterial spores. Biosens. Bioelectron. 25 https://doi.org/10.1016/j.bios.2010.03.021.

Goswami, P.P., Rotake, D.R., Singh, S.G., 2022. 2-D material enhanced ultrasensitive electrochemical sensing of Pro-BNP peptide towards the risk-assessment of human heart. Sensor. Actuator. B Chem. 357, 131382 https://doi.org/10.1016/J.SNB.2022.131382.

Hakim, M.M.A., Lombardini, M., Sun, K., Giustiniano, F., Roach, P.L., Davies, D.E., Howarth, P.H., De Planque, M.R.R., Morgan, H., Ashburn, P., 2012. Thin film polycrystalline silicon nanowire biosensors. Nano Lett. 12 https://doi.org/10.1021/nl2042276.

He, H., Zhang, Y.Y., Liu, J., Moore, D., Bao, G., Wang, Z.L., 2007. ZnS/silica nanocable field effect transistors as biological and chemical nanosensors. J. Phys. Chem. C 111. https://doi.org/10.1021/jp074772u.

Holzinger, M., Le Goff, A., Cosnier, S., 2017. Synergetic effects of combined nanomaterials for biosensing applications. Sensors. https://doi.org/10.3390/s17051010.

Huang, C.H., Huang, T.T., Chiang, C.H., Huang, W.T., Lin, Y.T., 2020. A chemiresistive biosensor based on a layered graphene oxide/graphene composite for the sensitive and selective detection of circulating miRNA-21. Biosens. Bioelectron. 164 https://doi.org/10.1016/j.bios.2020.112320.

Jacobs, C.B., Peairs, M.J., Venton, B.J., 2010. Review: carbon nanotube based electrochemical sensors for biomolecules. Anal. Chim. Acta 662, 105–127. https://doi.org/10.1016/j.aca.2010.01.009.

Jo, H., Gu, H., Jeon, W., Youn, H., Her, J., Kim, S.K., Lee, J., Shin, J.H., Ban, C., 2015. Electrochemical aptasensor of cardiac troponin i for the early diagnosis of acute myocardial infarction. Anal. Chem. 87 https://doi.org/10.1021/acs.analchem.5b02312.

Kim, K.H., Lara-Avila, S., He, H., Kang, H., Hong, S.J., Park, M., Eklöf, J., Moth-Poulsen, K., Matsushita, S., Akagi, K., Kubatkin, S., Park, Y.W., 2018. Probing variable range hopping lengths by magneto conductance in carbonized polymer nanofibers. Sci. Rep. 8 https://doi.org/10.1038/s41598-018-23254-0.

Kim, S., Lee, M.H., Wiwasuku, T., Day, A.S., Youngme, S., Hwang, D.S., Yoon, J.Y., 2021. Human sensor-inspired supervised machine learning of smartphone-based paper microfluidic analysis for bacterial species classification. Biosens. Bioelectron. 188 https://doi.org/10.1016/j.bios.2021.113335.

Kumar, R., Le, N., Tan, Z., Brown, M.E., Jiang, S., Reineke, T.M., 2020. Efficient polymer-mediated delivery of gene-editing ribonucleoprotein payloads through combinatorial design, parallelized experimentation, and machine learning. ACS Nano 14. https://doi.org/10.1021/acsnano.0c08549.

Lei, R., Wu, P., Li, L., Huang, Q., Wang, J., Zhang, D., Li, M., Chen, N., Wang, X., 2021. Ultrasensitive isothermal detection of a plant pathogen by using a gold nanoparticle-enhanced microcantilever sensor. Sensor. Actuator. B Chem. 338 https://doi.org/10.1016/j.snb.2021.129874.

Li, J., Yang, Z., Tang, Y., Zhang, Y., Hu, X., 2013. Carbon nanotubes-nanoflake-like SnS2 nanocomposite for direct electrochemistry of glucose oxidase and glucose sensing. Biosens. Bioelectron. 41 https://doi.org/10.1016/j.bios.2012.09.059.

Liu, Q., Aroonyadet, N., Song, Y., Wang, X., Cao, X., Liu, Y., Cong, S., Wu, F., Thompson, M.E., Zhou, C., 2016. Highly sensitive and quick detection of acute myocardial infarction biomarkers using In2O3 nanoribbon biosensors fabricated using shadow masks. ACS Nano 10. https://doi.org/10.1021/acsnano.6b05171.

Liu, Xinke, Hsu, S.P.C., Liu, W.-C., Wang, Y.-M., Liu, Xinrui, Lo, C.-S., Lin, Y.-C., Nabilla, S.C., Li, Z., Hong, Y., Lin, C., Li, Y., Zhao, G., Chung, R.-J., 2019. Salivary electrochemical cortisol biosensor based on tin disulfide nanoflakes. Nanoscale Res. Lett. 14, 189. https://doi.org/10.1186/s11671-019-3012-0.

Liu, Y., Yobas, L., 2014. Label-free specific detection of femtomolar cardiac troponin using an integrated nanoslit array fluidic diode. Nano Lett. 14 https://doi.org/10.1021/nl5032524.

Madriz, F.R., Jameson, J.R., Krishnan, S., Sun, X., Yang, C.Y., 2009. Circuit modeling of high-frequency electrical conduction in carbon nanofibers. IEEE Trans. Electron. Dev. 56 https://doi.org/10.1109/TED.2009.2022691.

Martucci, A., Leporatti, S., Singh Raghuwanshi, V., Garnier, G., Yu, B., Browne, C., 2020. Reversible pH responsive bovine serum Albumin hydrogel sponge nanolayer. https://doi.org/10.3389/fbioe.2020.00573.

Naganaboina, V.R., Singh, S.G., 2022. CdS based chemiresistor with Schottky contact: toxic gases detection with enhanced sensitivity and selectivity at room temperature. Sensor. Actuator. B Chem. 357 https://doi.org/10.1016/j.snb.2022.131421.

Ng, S.M., Krishnaswamy, P., Morissey, R., Clopton, P., Fitzgerald, R., Maisel, A.S., 2001. Ninety-minute accelerated critical pathway for chest pain evaluation. Am. J. Cardiol. 88 https://doi.org/10.1016/S0002-9149(01)01801-X.

Ouyang, M., Tu, D., Tong, L., Sarwar, M., Bhimaraj, A., Li, C., Coté, G.L., Di Carlo, D., 2021a. A review of biosensor technologies for blood biomarkers toward monitoring cardiovascular diseases at the point-of-care. Biosens. Bioelectron. https://doi.org/10.1016/j.bios.2020.112621.

Ouyang, M., Tu, D., Tong, L., Sarwar, M., Bhimaraj, A., Li, C., Coté, G.L., Di Carlo, D., 2021b. A review of biosensor technologies for blood biomarkers toward monitoring cardiovascular diseases at the point-of-care. Biosens. Bioelectron. 171 https://doi.org/10.1016/j.bios.2020.112621.

Pedregosa, F., Varoquaux, G., Gramfort, A., Michel, V., Thirion, B., Grisel, O., Blondel, M., Prettenhofer, P., Weiss, R., Dubourg, V., Vanderplas, J., Passos, A., Cournapeau, D., Brucher, M., Perrot, M., Duchesnay, É., 2011. Scikit-learn: machine learning in Python. J. Mach. Learn. Res. 12.

Peronnet, E., Becquart, L., Martinez, J., Charrier, J.P., Jolivet-Reynaud, C., 2007. Isoelectric point determination of cardiac troponin I forms present in plasma from patients with myocardial infarction. Clin. Chim. Acta 377. https://doi.org/10.1016/j.cca.2006.10.006.

Pohanka, M., 2018. Piezoelectric biosensor for the determination of tumor necrosis factor Alpha. Talanta 178. https://doi.org/10.1016/j.talanta.2017.10.031.

Prakash, M.D., Vanjari, S.R.K., Sharma, C.S., Singh, S.G., 2016. Ultrasensitive, label free, chemiresistive nanobiosensor using multiwalled carbon nanotubes embedded electrospun su-8 nanofibers. Sensors 16. https://doi.org/10.3390/s16091354.

Qian, T., Wang, Y., 2010. Micro/nano-fabrication technologies for cell biology. Med. Biol. Eng. Comput. 48 https://doi.org/10.1007/s11517-010-0632-z.

Reverberi, R., Reverberi, L., 2007. Factors affecting the antigen-antibody reaction. Blood Transfusion 5. https://doi.org/10.2450/2007.0047-07.

Rose, A., 1955. Space-charge-limited currents in solids. Phys. Rev. 97 https://doi.org/10.1103/PhysRev.97.1538.

Rusu, I., Turlacu, M., Micheu, M.M., 2022. Acute myocardial injury in patients with COVID-19: possible mechanisms and clinical implications. World J Clin Cases 10. https://doi.org/10.12998/wjcc.v10.i3.762.

Shen, Y., Tran, T.T., Modha, S., Tsutsui, H., Mulchandani, A., 2019. A paper-based chemiresistive biosensor employing single-walled carbon nanotubes for low-cost, point-of-care detection. Biosens. Bioelectron. 130 https://doi.org/10.1016/j.bios.2018.09.041.

Shown, I., Samireddi, S., Chang, Y.-C., Putikam, R., Chang, P.-H., Sabbah, A., Fu, F.-Y., Chen, W.-F., Wu, C.-I., Yu, T.-Y., Chung, P.-W., Lin, M.C., Chen, L.-C., Chen, K.-H., n. d. Carbon-doped SnS 2 nanostructure as a high-efficiency solar fuel catalyst under visible light. https://doi.org/10.1038/s41467-017-02547-4.

So, S., Khalaf, A., Yi, X., Herring, C., Zhang, Y., Simon, M.A., Akcakaya, M., Lee, S.H., Yun, M., 2021. Induced bioresistance via BNP detection for machine learning-based risk assessment. Biosens. Bioelectron. 175 https://doi.org/10.1016/j.bios.2020.112903.

Stafiniak, A., Boratyński, B., Baranowska-Korczyc, A., Szyszka, A., Ramiczek-Krasowska, M., Pramowska, J., Fronc, K., Elbaum, D., Paszkiewicz, R., Tłaczała, M., 2011. A novel electrospun ZnO nanofibers biosensor fabrication. Sensor. Actuator. B Chem. 160 https://doi.org/10.1016/j.snb.2011.09.087.

Supraja, P., Tripathy, S., Singh, R., Singh, V., Chaudhury, G., Singh, S.G., 2021. Towards point-of-care diagnosis of Alzheimer's disease: multi-analyte based portable chemiresistive platform for simultaneous detection of β-amyloid (1–40) and (1–42) in plasma. Biosens. Bioelectron. 186 https://doi.org/10.1016/j.bios.2021.113294.

Thiha, A., Ibrahim, F., Muniandy, S., Dinshaw, I.J., Teh, S.J., Thong, K.L., Leo, B.F., Madou, M., 2018. All-carbon suspended nanowire sensors as a rapid highly-sensitive label-free chemiresistive biosensing platform. Biosens. Bioelectron. 107 https://doi.org/10.1016/j.bios.2018.02.024.

Tripathy, S., Bhandari, V., Sharma, P., Vanjari, S.R.K., Singh, S.G., 2019. Chemiresistive DNA hybridization sensor with electrospun nanofibers: a method to minimize inter-device variability. Biosens. Bioelectron. 133 https://doi.org/10.1016/j.bios.2019.03.031.

Tripathy, S., Singh, S.G., 2021. Electrospun Mn2O3Nanofiber networks as bio-transducers: electrical characterization, modeling, and DNA sensing. IEEE Trans. Electron. Dev. 68 https://doi.org/10.1109/TED.2021.3059392.

Tripathy, S., Supraja, P., Mohanty, S., Sai, V.M., Agrawal, T., Chowdary, C.G., Taranikanti, M., Bandaru, R., Mudunuru, A.K., Tadi, L.J., Suravaram, S., Siddiqui, I. A., Maddur, S., Guntuka, R.K., Singh, R., Singh, V., Singh, S.G., 2021. Artificial intelligence-based portable bioelectronics platform for SARS-CoV-2 diagnosis with multi-nucleotide probe assay for clinical decisions. Anal. Chem. 93 https://doi.org/10.1021/acs.analchem.1c01650.

Voznyi, A., Kosyak, V., Opanasyuk, A., Tirkusova, N., Grase, L., Medvids, A., Mezinskis, G., 2016. Structural and electrical properties of SnS2 thin films. Mater. Chem. Phys. 173 https://doi.org/10.1016/j.matchemphys.2016.01.036.

Wang, G., Wang, K., Ren, J., Ma, S., Li, Z., 2022. A novel doublet-based surface plasmon resonance biosensor via a digital Gaussian filter method. Sensor. Actuator. B Chem. 360 https://doi.org/10.1016/j.snb.2022.131680.

Wang, J., Jiang, Z., Wei, Y., Wang, W., Wang, F., Yang, Y., Song, H., Yuan, Q., 2022. Multiplexed identification of bacterial biofilm infections based on machine-learning-aided lanthanide encoding. ACS Nano 16. https://doi.org/10.1021/acsnano.1c11333.

Wang, Y., Liu, T., Yang, M., Wu, C., Zhang, W., Chu, Z., Jin, W., 2021. A handheld testing device for the fast and ultrasensitive recognition of cardiac troponin I via an ion-sensitive field-effect transistor. Biosens. Bioelectron. 193 https://doi.org/10.1016/j.bios.2021.113554.

Wang, Z., Ye, J., Zhang, K., Ding, L., Granzier-Nakajima, T., Ranasinghe, J.C., Xue, Y., Sharma, S., Biase, I., Terrones, M., Choi, S.H., Ran, C., Tanzi, R.E., Huang, S.X., Zhang, C., Huang, S., 2022. Rapid biomarker screening of Alzheimer's disease by interpretable machine learning and graphene-assisted Raman spectroscopy. ACS Nano 16. https://doi.org/10.1021/acsnano.2c00538.

Yuan, Y.J., Chen, D.Q., Shi, X.F., Tu, J.R., Hu, B., Yang, L.X., Yu, Z.T., Zou, Z.G., 2017. Facile fabrication of "green" SnS2 quantum dots/reduced graphene oxide composites with enhanced photocatalytic performance. Chem. Eng. J. 313. https://doi.org/10.1016/j.cej.2016.11.049.

Zhang, K., Wang, J., Liu, T., Luo, Y., Loh, X.J., Chen, X., 2021. Machine learning-reinforced noninvasive biosensors for healthcare. Adv Healthc Mater. https://doi.org/10.1002/adhm.202100734.

Zhao, H., Du, X., Dong, H., Jin, D., Tang, F., Liu, Q., Wang, P., Chen, L., Zhao, P., Li, Y., 2021. Electrochemical immunosensor based on Au/Co-BDC/MoS2 and DPCN/MoS2 for the detection of cardiac troponin I. Biosens. Bioelectron. 175 https://doi.org/10.1016/j.bios.2020.112883.

Zubair Ansari, M., Khare, N., 2015. Thermally activated band conduction and variable range hopping conduction in Cu2ZnSnS4 thin films. J. Appl. Phys. 117 https://doi.org/10.1063/1.4905673.